48th AIAA Aerospace Sciences Meeting Including the New Horizons Forum and Aerospace Exposi
4 - 7 January 2010, Orlando, Florida

48th AIAA Aerospace Science Meeting
Jan. 4- 7, 2010, Orlando, Florida

AIAA 2010-1450

# A High Order Cut Cell Method for Numerical Simulation of Three Dimensional Hypersonic Boundary-Layer Transition with Finite Surface Roughness

Le Duan* and Xiaolin Zhong.†
University of California, Los Angeles, California 90095

Hypersonic boundary-layer transition can be affected significantly by surface roughness. Many important mechanisms which involve transition induced by arbitrary roughness are not well understood. Direct numerical simulation is broadly applied for investigating the roughness induced instability and transition in recent decade. But due to the complex computational geometry with embedded 3-D roughness, the use of body fitted curvilinear grids could prove to be very difficult. In our previous papers [44,45], we proposed a new high-order cut cell method to overcome the natural complexities in grid generation around curvilinear surface. The new algorithms of up to $O(h^4)$ accuracy have been derived and applied to simulate two-dimensional boundary-layer transition with finite surface roughness. Compared with two-dimensional roughness, the flow with three-dimensional isolated and distributed roughness is more complicated in analyzing and simulating. In this paper, we extend our previous new high order cut cell method to simulate three-dimensional hypersonic flow with finite surface roughness. The flow structure in three-dimensional boundary layer is investigated by using the new numerical approach.

## I. Introduction

Modeling of the roughness induced laminar-turbulence transition of boundary layer serves as a critical design issue for hypersonic vehicles, since transition can have a first order influence on their body lift and drag, stability and control, propulsion and proposer performance, heat transfer property, dynamic pressure loading et al. For example, swept wings are very critical mechanical parts for most commercial and military aircraft. It turns out that aerodynamics parameter may vary substantially after transition thus to understand the fundamental instability mechanisms in swept-wing flows is crucial considering its board application in aerospace design [1]. Another promising application of studying roughness induced transition is for heat protection. A spacecraft entering earth's atmosphere initially experiences a heating environment associated with a laminar boundary layer. Eventually as the vehicle surface become rougher, the boundary layer become turbulent and the heating rate at the surface can be increased by a factor of four or more. Thus the ability to understand and predict the roughness induced transition plays an essential role in thermal protection system (TPS) design process [2]. However, roughness

---

* Graduate Research Assistant, Department of Mechanical&Aerospace Engineering, University of California, Los Angeles, California 90095

† Professor, Department of Mechanical&Aerospace Engineering, University of California, Los Angeles, California 90095, Associate Fellow, AIAA

Copyright © 2010 by the American Institute of Aeronautics and Astronautics, Inc. All rights reserved.

induced laminar-turbulence transition in hypersonic boundary-layer is still poorly understood due to the limitation in experimental facilities and theoretical analysis.

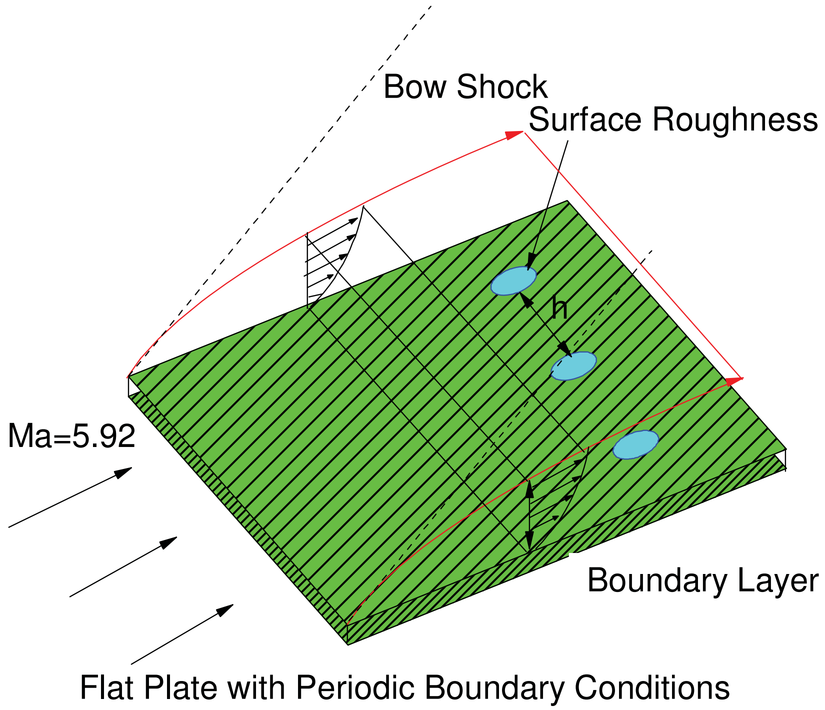

***Fig.1. A schematic of a hypersonic flow over flat plate with surface roughness induced boundary layer transition.***

Within the entire laminar-turbulence transition, the receptivity process involves the generation and excitation of instability wave (T-S waves) inside the boundary-layer under various external environmental perturbations [3]. The receptivity and transition process induced by surface roughness is one of the most studied fields in the last decades. The instability mechanisms associated with different kind of roughness are distinguished. Generally surface roughness which induces transition can be divided into three categories. Among those styles two-dimensional roughness(Spanwise variant three-dimensional roughness) have been well understood since the instability mechanisms inside is simple in analyzing and simulating both from the theoretical and experimental point of view. A well accepted conclusion is that both of the frequency of external free stream disturbance and surface roughness can affect the amplitude of T-S instable waves where a linear relationship between amplitude of T-S wave and height of roughness can be observed for small roughness [4].

Compared with two-dimensional roughness, isolated and distributed roughness is more complicated in analyzing in theory and there are still gap remaining both in numerical simulation and experiments. The three-dimensional roughness is observed to be more critical than two-dimensional roughness in introducing the instability mechanisms. It turns out that this kind of roughness may lead to bypass transition directly when the Reynolds number based on roughness height exceed a certain range [5]. Within this range, the roughness appears to have minor impact on transition. Recently, Balakumar [6] conduct numerically experiments on the transition process induced by isolated roughness with acoustic disturbance on supersonic boundary layer. His computational results show that the generation of T-S waves inside the boundary layer is mainly due to the acoustic waves while the roughness does not exert a significant influence on transition. Thus the above bypass process suggest us introduce a new instability mechanisms inside the boundary-layer other than traditional T-S instability, which is termed as transient growth.

Based on the instability waves generated from receptivity process, transient growth arises through the nonorthogonal nature of the Orr–Sommerfeld and Squire eigenfunctions. The largest effects come from the non-orthogonal superposition of slightly damped, highly oblique near streamwise T–S and Squire modes. These modes are subcritical with respect to the T–S neutral curve. The transient growth signature is essentially algebraic growth followed by exponential decay. A weak transient growth can also occur for two-dimensional or axisymmetric modes. Transient growth is therefore a candidate mechanism for many examples of bypass transition.

Transient growth was initially recognized by Ellingsen et al. [7] and by Landahl [8] as an inviscid mechanism producing an algebraic increase of kinetic energy in shear layer. Since its discovery, a number of investigators have made great contribution to its basic theoretical understanding. This theory was further developed by Trefethen et al [9], Henningson [10], Reshotko [11]. Recently, the spatial transient growth in 2-D boundary layers was addressed by Anderson et al. [12], Luchini [13] and Tumin et al. [14]. Andersson and Luchini consider the growth of stationary disturbances in non-parallel Blasius boundary layers at finite and infinite Reynolds number respectively. Tumin et al. consider the more general case of arbitrarily oriented disturbances at nonzero frequencies but are restricted to parallel-flow boundary layers. Both of their results show that the most significant transient growth is associated with stationary streamwise vortices. The plot of the spatial transient growth of zero-frequency, streamwise vortices of various streamwise wavenumbers calculated using the parallel-flow transient growth code by Tumin exhibit a distinguishable increasing modes from transitional T-S wave like exponential growth. Tumin and Reshotcko extended their former analytical techniques on receptivity prediction to the roughness induced transient growth in the context of linearly unstable T-S modes. By using biorthogonal eigenfunctions of the linear, quasiparallel disturbance equations, they are able to predict the stationary disturbances in the wake of an array of roughness elements.

Although the theoretical approaches have been making a good progress, there has not been much experiments designed to support the transient growth relating algebraic disturbance growth and the link with surface roughness. Prior to the development of transient growth theory, there are many experiments about surface roughness induced boundary layer transition, many of which were summarized in [15, 16]. One of the relevant experiments to current study comes from Reshotko and Leventhal [17]. They consider three different roughness levels: smooth (i.e., polished aluminum), low-amplitude roughness (nominally $R_k = 15$), and high-amplitude roughness (nominally) which placed in the subcritical region of a flat-plate boundary-layer. Measurements were obtained at four $x$ locations, 300, 400, 500, and 600 mm downstream of the leading edge, all along the plate centerline. What they found is that maximum amplitude of disturbance in the T-S subcritical region varies along streamwise direction in a clearly a non-exponential manner, whose characteristics are quite unlike those of T-S waves. When the growing disturbances they observed were filtered out through Fourier transformation, the component with lowest frequencies exhibits the strongest growth—exactly matching the prediction from transient-growth theory. Later, the experiment by Kendall [23] examine the evolution of a disturbance produced by an isolated roughness element.

The more recent experiment that directly supports the transient-growth theory is conducted by White et al. [18-21]. In white's experiments [21], The facility used in the experiments is the Case Wind Tunnel, an open-return facility with a $0.71*0.71*2.7m^3$ section and a maximum control speed $25m/s$. Disturbances are generated by a spanwise array of cylindrical roughness elements located 300 mm down-stream of the plate's physical leading edge. A clearly transient growth behavior for the streamwise evolution of steady disturbance energy $E_{rms}$ is observed. Under incompressible boundary environment, some parameters study associated with transient growth, such as the effects of roughness height and diameter on the steady disturbance energy are carried out. A main conclusion from their experiments is that the maximum amplitude of transient growth is linear proportional to square of height roughness.

By now there are limited reported numerical experiments related to boundary-layer transient growth with surface roughness. White's experiments are carried out by Fischer et al. [24,25] with spanwise periodic array of circular disks in incompressible boundary layer. In their simulation, the unsteady Navier-Stokes equations are integrated in by using the spectral element discretization in space and third-order, operator-splitting formulation in time. A parameter study is conducted for investigating the dependent of transient growth on geometric characteristics of the roughness distribution. The agreement between the experimental data and simulation result validate each other. They find that with sufficiently small roughness heights, a previously unknown trend about monotonic energy decay will appear for mode disturbance, which is consistent with Tumin's optimal growth. Piot et al. [26] performs a numerical simulation on flow around a swept cylinder in the presence of a micro-roughness array. Their spatial scheme is classical fourth-order accurate center explicit finite difference discretization, while temporal-wise is a compact explicit third-order accurate Runge-Kutta algorithm. The simulation shows that both the steady and unsteady waves are generated though the receptivity process induced by roughness and could be explained by LST analysis and biorthogonal decomposition. Rizzetta et al. [27] employ a high-order overset grid approach to simulate the subsonic flow past an array of distributed cylindrical roughness elements mounted on a flat plate. The $R_k = 202$ case shows a exponential growth of turbulence energy in the steamwise direction, which may ultimately lead to transition.

For problems having complex computational geometry, as might occur in the transition problems induced by isolated/distributed roughness, use of body fitted curvilinear gird could prove to be very difficult due to natural complexities in grid generation. Consequently, a Cartesian cut cell method should be used for its advantage in generating and implementing numerical schemes. Cut cell methods can take full advantage of fast computer architectures like vector or parallel computers and could serve as a very flexible method for simulating flow around complex geometries. In the retrospect of the cut cell method, it was first used in the context of solving the equations of transonic potential flow by Purvis and Burkhalter [28]. Then it is used to calculate steady compressible flows by Clarke et al. [29]. Among those methods, a restriction on time step will arise when dealing with the relatively small irregular cell formed by irregular cutting of boundaries. This restriction will significantly delay the time advance thereby make the object system of equations become too stiff to solve. Thus the major issues for our numerical algorithm is on how to design a method that while relax the time step, can maintain the result accuracy, stability, and conservation inside the irregular cells at the fluid-body interface simultaneously.

Many innovative methods were developed to resolve this problem. Berger and Leveque [30] use rotating box method to address the small cell problems. Colella et al. [31-33] uses flux-redistribution procedures, and Quirk [34], Shyy [35] uses cell merging skill to get numerical stability. However, all the cut cell methods with different treatments for the boundary can be found are of first or second order, which is not sufficient in numerically predicting laminar-turbulent boundary transition. Later a series of the new cut cell method were developed equipped with high-order features. Shyy et al. [37] extend its old method to fourth order with merging cell skill. But the reconstruction of flux procedure is relatively expensive thus slowing down the computational efficiency. Colella et al. [38] developed a fourth order accurate finite volume method combined with a local mesh refinement for discretezating Poisson's equation in a rectangular domain. This kind of method will be extremely tedious in implementing for irregular domain. Fedkiw et al. [39] also presented a fourth order finite difference method for solving the Laplace and Heat equation on arbitrary domain by using ghost fluid method.

In this paper, we present a high-order cut cell method to simulate the roughness induced transient growth and transition in three-dimensional hypersonic boundary layer. An array of roughnesses with smooth surface is placed in the spanwise direction at the flat plate 0.185m downstream from the leading edge. The spanwise distance between two close roughnesses is 0.01m. The bow shock generated from leading edge of flat plate will be treated as a boundary condition and discretizated based on Zhong's [41] fifth-order finite difference flux split method and shock fitting method. To extend our original two-dimensional cut cell method, we calculate the irregular points in three dimensional geometry and extend corresponding numerical scheme. A local refinement of a cut cell may be incorporated to obtain a method that is of third or higher order accuracy.

## II. Governing Equations

The governing equations for the numerical simulation of hypersonic boundary layer transition are the three-dimensional Navier–Stokes equations. We assume that we are dealing with Newtonian fluids with perfect gas assumption and isothermal wall condition. The governing equations can be written in the following conservation-law form in the Cartesian coordinates,

$$\frac{\partial U}{\partial t}+\frac{\partial F_j}{\partial x_j}+\frac{\partial F_{vj}}{\partial x_j}=0 \tag{1}$$

where $U$, $F_j$ and $F_{vj}$ are the vectors of flow variables, convective flux, and viscous flux in the $jth$ spatial direction respectively, i.e.,

$$U=\{\rho,\rho u_1,\rho u_2,\rho u_3,e\} \tag{2}$$

$$F_j = \begin{Bmatrix} \rho u_j \\ \rho u_1 u_j + p\delta_{1j} \\ \rho u_2 u_j + p\delta_{1j} \\ \rho u_3 u_j + p\delta_{1j} \\ (e+p)u_j \end{Bmatrix} \tag{3}$$

$$F_{vj} = \begin{Bmatrix} 0 \\ \tau_{1j} \\ \tau_{2j} \\ \tau_{3j} \\ \tau_{jk}u_k - q_j \end{Bmatrix} \tag{4}$$

In this paper, only perfect-gas hypersonic flow is considered, i.e.,

$$p = \rho RT \tag{5}$$

$$e = \rho(C_V T + \frac{1}{2}u_k u_k) \tag{6}$$

$$\tau_{ij} = \mu(\frac{\partial u_i}{\partial x_j} + \frac{\partial u_j}{\partial x_i}) + \delta_{ij}\lambda\frac{\partial u_k}{\partial x_k} \tag{7}$$

$$q_j = -k\frac{\partial T}{\partial x_j} \tag{8}$$

where $R$ is the gas constant. The specific heat $C_V$ is assumed to be constant with a given ratio of specific heats $\gamma$. The viscosity coefficient $\mu$ can be calculated by Sutherland's law in the form:

$$\mu = \mu_r \left(\frac{T}{T_0}\right)^{3/2} \frac{T_0 + T_S}{T + T_S} \tag{9}$$

Where $\mu_r = 1.7894\times10^{-5} Ns/m^2, T_0 = 288.0K, T_S = 110.33K$ and $\lambda$ is assumed to be $-2/3\mu$. The heat conductivity coefficient $k$ can be computed through a constant Prantl number $\mathrm{Pr}$.

## III. Numerical Methods

### A. Grids Generation and Definition

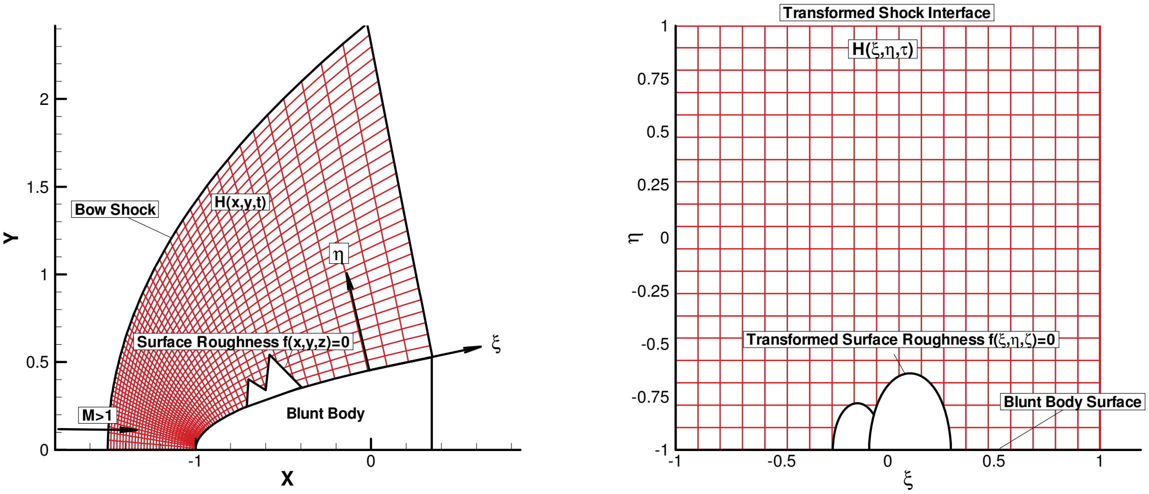

***(a)*** ***(b)***

***Fig.2. Hypersonic boundary layer transition with surface roughness a), hypersonic flow over blunt body with surface roughness b), the computational domain with roughness after the transformation and Cartesian cut cells generation.***

A schematic of roughness induced hypersonic boundary layer transition is shown in Figure 2. The roughness surface is a close curve and is governed by the equation,

$$\Gamma : f(x, y, z) = 0 \tag{10}$$

It is possible that there is not an analytical equation applicable to represent some special roughness e.g. real arbitrary roughness in hypersonic vehicle surface. In these cases a set of $n$ discrete coordinate points $\{(x_1, y_1, z_1), (x_2, y_2, z_2), ..., (x_n, y_n, z_n)\}$ can be obtained by scanning the physical roughness surface. With the roughness data we can reconstruct the roughness surface for simulation by using high order piecewise continuous and differentiable Lagrange interpolation polynomials.

The shock fitting method is used to compute the unsteady boundary layer transition. The governing Eqs. (1) – (8) and (10) in the physical domain are transformed into a regular computational domain bounded by oscillating shock and flat plate boundary. Under the computational coordinate system, the body fitted grids are represented by a curvilinear three-dimensional coordinates $(\xi, \eta, \varsigma, \tau)$ along the grid lines. The unsteady movement of the bow shock is treated as the computational upper bound at $\eta = \eta_{\max}$, which is time dependent. The other grid lines $\xi = const$ and $\varsigma = const$ remains stationary while computing. The coordinate transformation is defined by:

$$\begin{cases} \xi = \xi(x, y, z) \\ \eta = \eta(x, y, z, t) \\ \varsigma = \varsigma(x, y, z) \\ \tau = t \end{cases} \longrightarrow \begin{cases} x = x(\xi, \eta, \varsigma, \tau) \\ y = y(\xi, \eta, \varsigma, \tau) \\ z = z(\xi, \eta, \varsigma, \tau) \\ t = \tau \end{cases} \tag{11}$$

where $(x, y, z, t)$ is defined under Cartesian coordinate system.

Eq. (11) can be substituted into the governing Eq. (1), which may lead to a system of transformed equations in the computational domain $(\xi, \eta, \zeta, \tau)$ as

$$\frac{1}{J}\frac{\partial U}{\partial \tau} + \frac{\partial E'}{\partial \xi} + \frac{\partial F'}{\partial \eta} + \frac{\partial G'}{\partial \zeta} + \frac{\partial E_V{}'}{\partial \xi} + \frac{\partial F_V{}'}{\partial \eta} + \frac{\partial G_V{}'}{\partial \zeta} + U\frac{\partial (1/J)}{\partial \tau} = 0 \tag{12}$$

where

$$E' = \frac{F_1\xi_x + F_2\xi_y + F_3\xi_z}{J} \tag{13}$$

$$F' = \frac{F_1\eta_x + F_2\eta_y + F_3\eta_z + U\eta_t}{J} \tag{14}$$

$$G' = \frac{F_1\zeta_x + F_2\zeta_y + F_3\zeta_z}{J} \tag{15}$$

$$E_v{}' = \frac{F_{v1}\xi_x + F_{v2}\xi_y + F_{v3}\xi_z}{J} \tag{16}$$

$$F_v{}' = \frac{F_{v1}\eta_x + F_{v2}\eta_y + F_{v3}\eta_z}{J} \tag{17}$$

$$G_v{}' = \frac{F_{v1}\zeta_x + F_{v2}\zeta_y + F_{v3}\zeta_z}{J} \tag{18}$$

Where $\xi_x, \xi_y, \xi_z, \eta_x, \eta_y, \eta_z, \varsigma_x, \varsigma_y, \varsigma_z$ are transformation metrics and $J$ is Jacobean matrix of coordinate transformation defined by

$$J = \frac{\partial(\xi, \eta, \varsigma)}{\partial(x, y, z)} \tag{19}$$

The surface roughness is also transformed into the computational domain and can be represented as

$$f(\xi(x, y, z), \eta(x, y, z, t), \varsigma(x, y, z)) = 0 \tag{20}$$

The grids transformation metrics and the Jacobean matrix could be calculated through applying derivative chain rule into the relation of Eq. (11). With the coordinate transformation, uniform distributed grids could be generated in the computational domain where in reality the grids distribution in physical domain is non-uniform distributed.

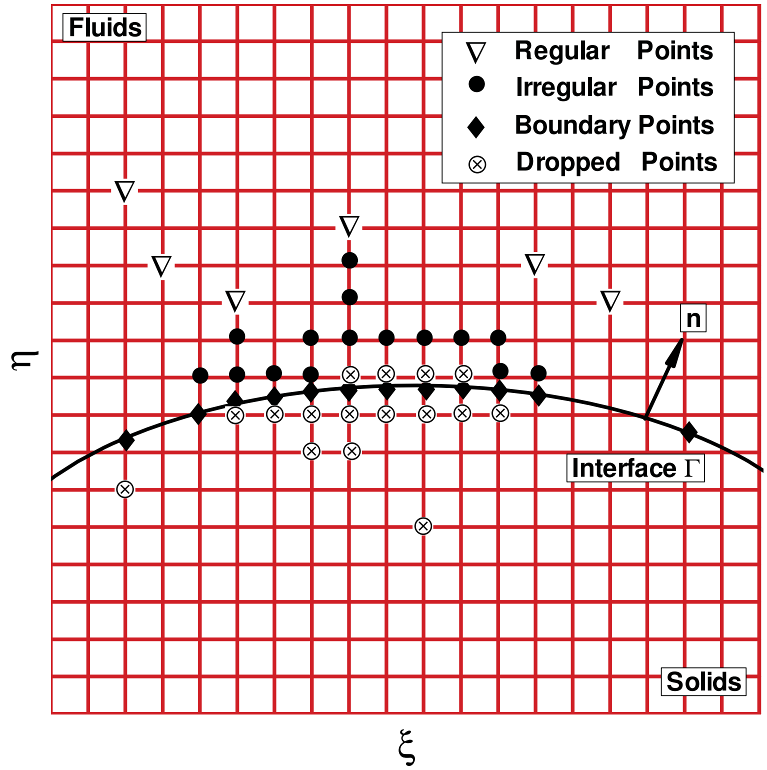

***Fig.3. Definition of grids for high-order cut-cell method in a coordinated plane*** $(\xi,\eta)$ ***(Other plane are similar).*** $\nabla$ ***is regular point,*** $\otimes$ ***is dropped point,*** $\Diamond$ ***is boundary point and*** ● ***is irregular point.***

Smooth body-fitted uniformly distributed grids are generated in the regular computational domain without roughness as shown in the Figure 2(b). Some of the Cartesian cells may cut by the roughness boundary, which leads to irregular Cartesian cells. The roughness geometry should be transformed into $(\xi,\eta,\varsigma,\tau)$ coordinate plane following the Eq. (10) while computing the metrics associated with roughness boundary.

Four different kinds of grids located in the vertex of those Cartesian cells are defined and different numerical algorithms are implemented. They are regular points, irregular points, boundary points, and dropped points as shown in Figure 3. The intersections of roughness interface and grid lines are defined as boundary points. The other points produced by intersections of grid lines themselves are termed as regular points, irregular points and dropped points respectively. The criteria for distinguishing those are depending on their minimum distances to the solid wall. If the grids points are adjacent to a boundary point with a distance smaller than a pre-specified critical ratio $\Theta$ in wall-normal or streamwise direction, they are defined as dropped points and are took off from the grid stencil in corresponding direction, which is terms as “dropped direction”. The points are abandoned in the “dropped direction” only, they may be included in finite difference stencils in directions that are not defined as “dropped”. In the third and fourth order simulation, the critical ratio $\Theta$ is selected to be $0.5\Delta h$ and $\Delta h$ respectively where desirable stable solution can be obtained as shown in following sections.

All the points in the solid side of computational domain can be defined as dropped points as well. They don't participant any numerical calculation in later stage. For those points whose finite difference stencil may include boundary points, they are defined as irregular points. Then the left points which cover the entire domain are defined as regular points since they are relatively far away from boundary points, where a standard uniform finite difference approach can be applied.

### B. Cut-Cell Method and Numerical Scheme

Based on different grids definition in the computational domain, the steps to derive the numerical scheme for both irregular and regular points are described as following.

### Regular Points

In the discretization of the Navier-Stokes equations at regular points, spatial derivatives in the streamwise ($\xi$) and wall-normal ($\eta$) directions are modeled by a fifth-order finite difference scheme. The flow variables behind the shock are determined by the Rankine-Hugoniot relations across the shock and a characteristic compatibility equation behind the shock. The velocity of shock front and acceleration of shock front could be written as the relation,

$$\begin{cases} \dfrac{\partial H}{\partial \tau} = H_\tau \\ H_{\tau\tau} = H_{\tau\tau}(\xi, \zeta, H, \tau, P_\infty, Ma_\infty, \rho_\infty) \end{cases} \tag{21}$$

$H_{\tau\tau}(\xi, \zeta, H, \tau, P_\infty, Ma_\infty, \rho_\infty)$ is a relation determined by time and the condition $P_\infty, Ma_\infty, \rho_\infty$. With time advancing in computation, the shock shape as well as the physical domain is updated in each simulation step according to equation (20). The details about derivation of the shock fitting formulas and numerical methods can be found in Zhong (*1998*).

The transformed Eq. (12) is discretized by a high-order uniform finite difference method. In the inviscid flux term, the Jacobian matrix contains both positive and negative eigenvalues, thus for obtaining more stable computation, two sets of schemes are employed to calculate viscous and inviscid flux term separately. A fifth-order upwind scheme combined with a local Lax-Friedrichs flux (LLF) split scheme is used for discretizing the inviscid flux derivatives, while a six order central scheme is used to discretize the viscous flux derivatives.

The inviscid flux term in Eq. (12) can be divided into two parts with pure negative and position values as

$$F' = F'^{+} + F'^{-} \tag{22}$$

To obtain Eq. (22), a general method is to choose a sufficient large parameter $\lambda$, like

$$\lambda = \frac{|\nabla \eta|}{J}(\sqrt{(\varepsilon c)^2 + u^2} + c \tag{23}$$

where $c$ is the speed of sound, $\varepsilon$ is a small variable which introduce smoothness of the flux splitting, and $u$ can be calculated by

$$u' = \frac{\eta_x u + \eta_y v + \eta_z w + \eta_t}{|\nabla \eta|} \tag{24}$$

$\lambda$ could be chosen to be larger than any of the absolute eigenvalue of $F'$.Then $F'^+$, $F'^-$ could be defined as

$$\begin{cases} F'^- = \frac{1}{2}(F' - \lambda U) \\ F'^+ = \frac{1}{2}(F' + \lambda U) \end{cases} \tag{25}$$

Since $F'^-$ and $F'^+$ contains only pure negative and positive value respectively, the fifth-order explicit upwind scheme could be used to discretize their derivatives in order to improve the overall computational stability. A finite difference equation for first order derivatives could be written as

$$\frac{\partial F'^+}{\partial \xi} = \frac{1}{\Delta h} \sum_{k=-3}^{3} a_{i+k} F'^+_{i+k} - \frac{\alpha}{6!} \left( \frac{\partial F'^+}{\partial \xi} \right)_i^6 + \ldots\ldots \tag{26}$$

where $\Delta h$ is the size of spatial grids. The coefficients can be calculated by using Taylor expansion as follows:

$$\begin{cases} a_i = \frac{1}{b}(-\frac{5}{3}\alpha) \\ a_{i\pm1} = \frac{1}{b}(\pm 45 + \frac{5}{4}\alpha) \\ a_{i\pm2} = \frac{1}{b}(\mp 9 - \frac{1}{2}\alpha) \\ a_{i\pm3} = \frac{1}{b}(\pm 1 + \frac{1}{12}\alpha) \qquad b = 60 \end{cases} \tag{27}$$

When $\alpha < 0$ the scheme is upwind and when $\alpha = 0$, the scheme is sixth-order central difference, which is used to discretize the viscous terms. Combined with cut cell method for boundary treatment, the spatial discretization towards Eq. (12) leads a system of ordinary differential equation. For steady problem, a first-order Euler scheme is used to discretize the system of ODEs, which in turn lead to a system of linear equations. Final solution can be obtained through temporal integration. The stability analysis for the high-order finite difference method can be found in Zhong's paper (*1998*).

### Irregular Points

Contrary to the standard fifth-order finite-difference schemes used for regular points, special treatment is needed in the discretization of the governing equations for the irregular points because boundary points are included into the finite difference stencil. Fig 4. shows a schematic of a grid stencil for irregular points near the boundary. In this figure, grid points $\xi_2$ and $\xi_3$ are irregular points, $\xi_1$ is a boundary point, while the grid point between $\xi_1$ and $\xi_2$ is a dropped point because it is too close the boundary point. The dropped point is removed from the stencil for the irregular point schemes. The rest of the grid points are regular points. For example, for a local third-order finite-difference approximation at the irregular point $\xi_2$, the grid stencil consists of the following five grid points: $\xi_1$, $\xi_2$, …, $\xi_5$. The grid spacing between the points involved are not uniform because

$$\sigma = \frac{\theta}{\Delta h} \neq 1 \tag{28}$$

where $\theta$ is the spacing between $\xi_1$ and $\xi_2$, and $\Delta h$ is the uniform grid spacing of the regular grid. Therefore, a non-uniform-grid finite difference schemes are needed for irregular points.

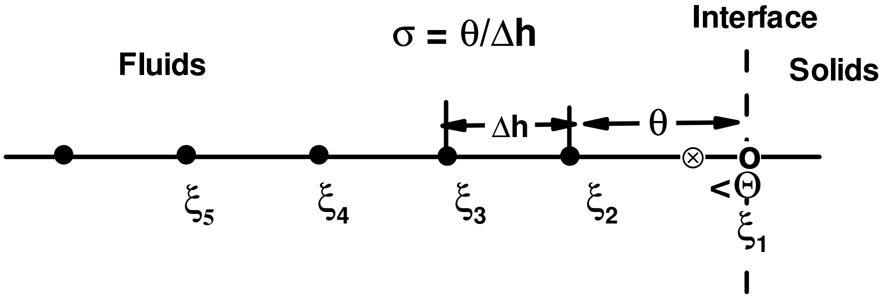

***Fig. 4. A schematic of a grid stencil for an irregular point with*** $p=3$ , $q=5$ ***and*** $\Omega_3^{\xi}=\{\xi_2,\xi_3\}$, $\theta$ ***is non-uniform grid spacing after removing a dropped point,*** $\Delta h$ ***is the normal grid spacing,*** ⊗ ***represents the dropped point,*** O ***represents the boundary point, and*** ● ***represents irregular and regular points.***

It is assumed that $p$ is the local order of accuracy in boundary of the simulation. In order to maintain a $(p+1)-th$ order global accuracy for the distretization of both the inviscid and viscous flux terms, all local non-uniform schemes for irregular points need to be at least $p-th$ order accuracy. In our construction of high-order cut-cell scheme, if a grid stencil with a number of $q$ grids is used for discretizing regular points near the boundary in each direction of the computational domain, there are $\lfloor q/2 \rfloor$ irregular points near a boundary surface. Figure 4 shows the case of a third-order scheme with $q=5$, where there are two irregular points $\xi_2$ and $\xi_3$. We denote the collection of all irregular points near this boundary in one direction as set $\Omega_p^{\xi}$, where the superscript represents the direction of the stencil and the subscript represents the local order of schemes at this point.

## Viscous Term in Irregular Points

The general formulation of a non-uniform-grid finite-difference scheme for computing the viscous terms for an irregular point $\xi_i$ of $\Omega_p^\xi$ can be written in the following form:

$$\left(\frac{\partial F_v^{'}}{\partial \xi}\right)_i = \frac{1}{\Delta h}\sum_{k=1}^{q} a_{i,k}(\sigma)F_{v,k}^{'} - \frac{C(\Delta h)^{q-1}}{q!}\left(\frac{\partial F_v{'}}{\partial \xi}\right)_i^{q-1} \qquad \text{for } \xi_i \in \Omega_p^\xi \text{ where } i = 2,3,...,\lfloor q/2 \rfloor + 1 \quad (29)$$

The subscripts of coefficient $a_{i,k}$ stand for the $k-th$ coefficient for the $i-th$ irregular point as defined for the case of $p$=3 and $q=5$ (Fig. 4). The coefficient $a_{i,k}$ is function of $\sigma$, which is defined in Eq.28 , and $C$ is a constant.

## Inviscid term in irregular points

Similar to the local algorithms for the viscous terms at irregular points, a non-uniform-grid high-order upwind scheme is used to discretize the inviscid fluxes, $F^{'+}$ and $F^{'-}$, as defined in Eq.25. For every irregular grid point, there are several possible grid stencils for finite-difference approximation of the flux derivatives of the same accuracy order. Different choices of stencils for these boundary closure schemes lead to different stability characteristics for the overall algorithm. Since $F^{'+}$ and $F^{'-}$ have either all positive or all negative eigenvalues, local grid stencils for finite-difference approximation of the flux derivatives are chosen so that the discretization for the fluxes are upwind biased, while maintaining high-order accuracy. Therefore, for a given irregular grid point, the stencil for $F^{'+}$ may be different from the stencil for $F^{'-}$. In addition, a grid stencil for these fluxes may or may not include the boundary point.

The non-uniform-grid finite-difference schemes for the inviscid flux terms of positive and negative eigenvalues can be written as

$$\left(\frac{\partial F^{'+}}{\partial \xi}\right)_i = \frac{1}{\Delta h}\sum_{k=1}^{q} b_{i,k}^{+} F^{'+}_{k} \qquad \text{for } \xi_i \in \Omega_p^\xi \text{ where } i = 2,3,...,\lfloor q/2 \rfloor + 1 \quad (30)$$

$$\left(\frac{\partial F^{'-}}{\partial \xi}\right)_i = \frac{1}{\Delta h}\sum_{k=1}^{q} b_{i,k}^{-}(\sigma) F^{'-}_{k} \qquad \text{for } \xi_i \in \Omega_p^\xi \text{ where } i = 2,3,...,\lfloor q/2 \rfloor + 1 \quad (30)$$

The stencil contains a total of $q$ grid points as shown in Fig. . The subscripts of coefficients $b_{i,k}^{+}$ and $b_{i,k}^{-}$ stand for the $k-th$ coefficient for the $i-th$ irregular point as defined in Fig. 5. The upwind schemes are represented by different sets of coefficients of the two formulas above. Because the upwind bias stencil used for $\frac{\partial F^{'+}}{\partial \xi}$ does not include the boundary point, the coefficients $b_{i,k}^{+}$ is not a function of $\sigma$ defined in Eq.25. On the other hand, $b_{i,k}^{-}$ is a function of

$\sigma$ because the upwind stencil for $\frac{\partial F'^{-}}{\partial \xi}$ includes the boundary point. The coefficients for each upwind schemes above can be calculated following the same general formulas as in the previous section.

**Boundary points**

As shown in Fig. 3, boundary points are the marker points located at the intersection between the roughness surface and grid lines. The governing equations are not solved at these points. However, flow variables at these points are needed for finite-difference algorithms of the irregular points near the roughness surface. The solid interface imposes the non-slip and non-flow-through conditions for flow velocities at the boundary points. Depending on the actual thermal conditions of the solid surface, either an isothermal or adiabatic wall can be specified. In this paper, only the isothermal wall is considered. In this case, both the velocities and temperature of the boundary points are specified by the wall boundary conditions. The local pressure on the solid surface (boundary points) needs to be computed by the local flow conditions near the wall.

There are several approaches to compute the pressure at the boundary points. One approach is to integrate a local wall-normal momentum equation to obtain the wall pressure. We can also use an approximation assumption of zero pressure gradient at the wall to determine the pressure there. In a previous paper, Zhong used a fifth-order polynomial extrapolation to determine the wall pressure [13]. Satisfactory results have been obtained with this approach. We follow the extrapolation approach of Zhong [13] to determine the pressure at the boundary points.

In computing pressure at the boundary points, the polynomial extrapolation is required to have comparable order of accuracy as that of the interior schemes in order to maintain the expected global accuracy. To maintain a $(p+1)-th$ order global accuracy of the upwind schemes developed in the last sections, it is desirable to have at least $p-th$ order of accuracy for the extrapolation for the boundary points.

Since a boundary point is formed by the intersection of the roughness interface with one of the grid lines, the extrapolation is conducted along the direction of the same grid line. We use the grid line along the $\xi$ direction as an example. The methods can be applied the other directions similarly. In two and three-dimensional cases, there is options of either constructing the extrapolation along the direction normal to the solid interface, or doing it along the grid lines. Though either method can be used in multi-dimensional problems, the latter approach is used in this paper. In this case, the determination of pressure at the boundary points is a one-dimensional extrapolation along one of the grid lines. The one-dimensional stencil of Fig. 4, which involves non-uniform grid spacing $\theta$, is used to derive the extrapolation formulas for the pressure at the boundary point. For example, for the case of four point extrapolation shown in Fig. 4, pressure at the boundary point $p(\xi_1)$ is obtained by a third degree polynomial interpolating through the following four interior pressures: $p(\xi_2)$, $p(\xi_3)$, $p(\xi_4)$, and $p(\xi_5)$. The grid spacing between neighboring grid points is a constant value of $\Delta h$, with the exception that the distance between the first and second points are $\theta$. If there is a dropped point in the stencil, the dropped point is not used in the extrapolation calculations.

For current three-dimensional problems, the high-order extrapolation along the $\xi$ or $\eta$ or $\zeta$ direction is employed to extrapolate pressure from the interior domain into the boundary. A total of $p$ grid points in the direction associated with the boundary point are chosen to be included in the extrapolation stencil. Again, dropped points are not included in the extrapolation stencil. This procedure can prevent the small cell problem of producing numerical instability near the solid boundary.

## Dropped Points

In this paper, in order to avoid the small cell problem, a grid point is designated as a dropped point if its distance from a neighboring boundary point along a grid line is smaller than a pre-determined value $\Theta$. The dropped point, which is associated with a grid direction, is removed in the finite-difference grid stencil along the grid line for the irregular points near the boundary. On the other hand, a grid point may become a dropped point in one direction, but remain a regular or irregular point in another. For example, point $P_1$ in Fig. 5 is a dropped point in the $\xi$ direction, but a regular point in the $\eta$ direction. In this case, the flow variables at point $P_1$ are not used in finite difference formulas for derivatives in the $\xi$ direction. However, the flow variables at the same grid point are needed for finite difference formulas for derivatives in the $\eta$ direction. The flow variables at this dropped point $P_1$ are obtained by the interpolation of a stencil along the $\xi$ direction.

For a grid point which is a regular or irregular point in one direction, but a dropped point in another, finite difference schemes along the former direction may include this point in its stencil. As shown in Fig. 4 for the case of $p=3$, the finite-difference stencil for an irregular point $Q$ located at $(\xi_i,\eta_j)$ contains five points in the $\eta$ direction, which are in set $\Omega_Q=\{(\xi_i,\eta_{j+2}),\ (\xi_i,\eta_{j+1}),\ (\xi_i,\eta_j),\ (\xi_i,\eta_{j-1}),\ (\xi_i,\eta_{j-2})\}$. There are two dropped points along the $\xi$ direction in this set of stencil $\Omega_Q$: point $P_1$ at $(\xi_i,\eta_{j-1})$ and point $P_2$ at $(\xi_i,\eta_{j-2})$. If the points $P_1$ and $P_2$ are removed from the stencil used in the calculations of flux terms $\partial F' / \partial\eta$ and $\partial F_v' / \partial\eta$ in $Q$, the stencil set $\Omega_Q$ needs to be shifted two grids down to include $(\xi_i,\eta_{j-3})$ and $(\xi_i,\eta_{j-4})$ to maintain the accuracy. In this case, the resulting stencil for $Q$ may contain a significantly large interval $\theta$ compared with the normal grid spacing $\Delta h$, which may lead to a deterioration of accuracy of the method. Therefore, we maintain the original grid stencil $\Omega_Q$, which includes points $P_1$ and $P_2$, along the $\eta$ direction for point $Q$. We calculate the flow variables of these two dropped points by interpolation along the $\xi$ direction.

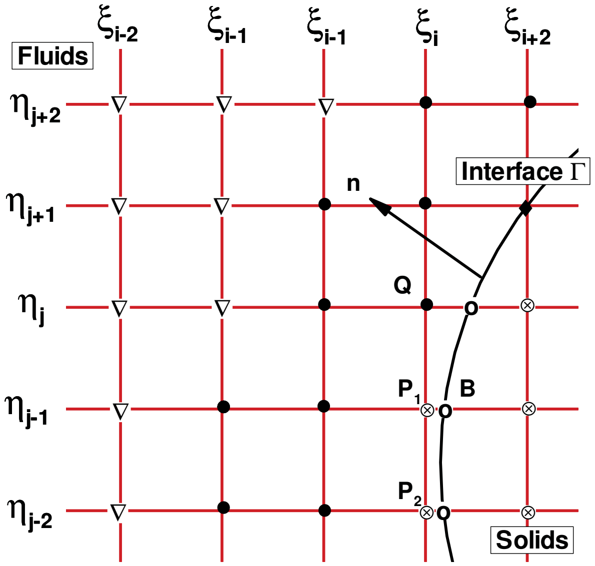

***Fig. 5. An example of a grid point, such as point $P_1$ and point $P_2$, which is a regular or irregular point in one direction, but a dropped point in another for the case of $p = 3$: $\nabla$ represents regular points, $\otimes$ dropped points, O boundary points, and ● irregular points.***

For the case of $p = 3$ for point $P_1$, a third-order polynomial interpolation along the $\xi$ direction is employed to compute the flow variables at this point. The interpolation is carried out along the $\xi$ direction, which is along the direction where the point is dropped. For $p = 3$ as shown in Fig. 5. the interpolation stencil for point $P_1$ is set $\Omega_P = \{(\xi_{i-1}, \eta_{j-1}),\ (\xi_{i-2}, \eta_{j-1}),\ B\}$, where $B$ represents the boundary point. For higher order method, the order of interpolation needs to be increased accordingly. For $p = 4$, a fourth order interpolation should be used. For a general case of $p - th$ order methods at the boundary, a total of $p-1$ adjacent grid points and exactly one boundary point along the $\xi$ direction are chosen as the interpolation stencil. The interpolant can be written as

$$\tilde{U}(\xi_{p_1}) = \sum_{n=1}^{p}\left(\prod_{l=1,l\neq n}^{p}\frac{\xi_{p_1}-\xi_l}{\xi_n-\xi_l}\right)U_n \qquad (31)$$

Where $\xi_{p_1}$ is the $\xi$ coordinate of dropped point, $\{U_i, i = 1..p\}$ is conservative flow variables at the grid points of the interpolation stencil.

Similar interpolation procedures can also be carried out if a point is designated as a dropped point in the $\eta$ and $\zeta$ direction, but is an irregular or regular point in the $\xi$ direction. If a grid point is designated as a dropped point in all the $\xi$ , $\eta$ and $\zeta$ directions, there is no need to do interpolations because this point is removed from the calculations of both directions.

## IV. Steady Base Flow over a three-dimensional flat plate without Roughness

A test case for flow over a three-dimensional flat plate with Mach number 5.92 without roughness is conducted. The numerical results could serve as a benchmark for filtering out steady mean flow components from the flow field with roughness generated perturbations. The ambient flow conditions are following Maslov's experiment (*2001*) as,

$$\begin{cases} P_r = 0.72, R_\infty = \rho_\infty * u_\infty / \mu_\infty = 1.32\times10^6 / m \\ M_\infty = 5.92, T_\infty = 48.69K, P_\infty = 742.76Pa \end{cases} \tag{32}$$

Where $M_\infty$ is Mach number, $T_\infty$ is temperature, $P_\infty$ is pressure, $P_r$ is Prantle number and $R_\infty$ is unit Reynolds number. The flat plate is assumed to be isothermal with fixed temperature $T_w = 350.0K$ .

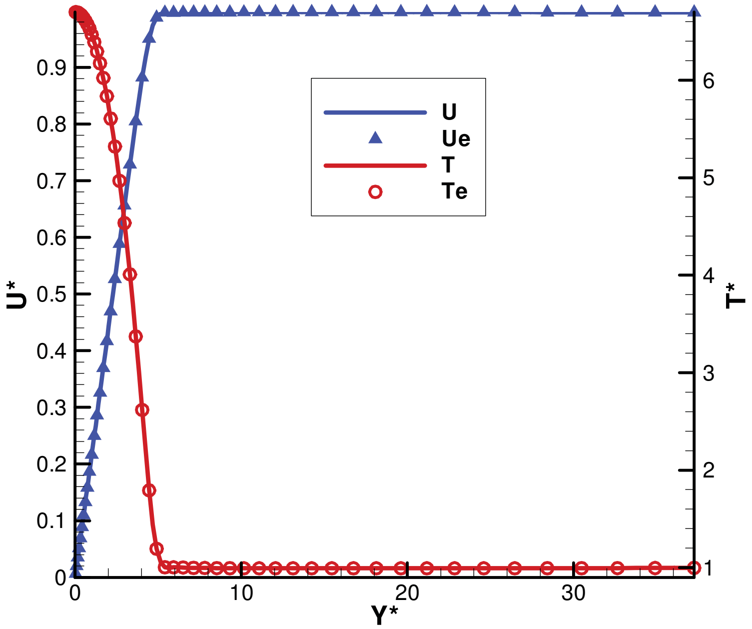

***Fig.6. Temperature and wall normal velocity long a wall-normal grid line which is originated from a point located at*** $x = 0.1676m$ ***and*** $z = 0.05m$ ***on the plate surface.***

The steady mean flow solutions are calculated by using a high-order shock fitting method discussed in section III. But in the leading edge of the flat plate, there is a singularity when high-order shock fitting method is implemented. Thus a second-order TVD shock-capturing method is employed to calculate the flow field in the tip of flat plate. The computational domain for TVD starts from a very short distance downstream of the leading edge which is divided to $241\times121\times16$ grids. The spatial discretization of TVD scheme following Lee et al. (*1993*) is applied toward Eq. (12) and leads to semi-discrete system of ordinary differential equations, which are solved by using fourth-order Runge-Kutta method.

The computational domain for the high-order shock-fitting methods starts at $x = 0.003m$ and ends at $x = 1.68784m$. In actual simulations, the computational domain is divided into 30 zones, with total of 5936 grid points in the stream wise direction, 121 points in the wall-normal direction and 6 points in the span wise direction. As mentioned above, the second zone uses the results of the first zone of second-order TVD scheme as the inlet condition. The later zone used the interpolation of former zone's data as the inlet condition.

Figure 6 shows the streamwise velocity profile and temperature profiles in the wall-normal direction at the location of $x = 0.1676m$ and $z = 0.005m$ .The current numerical solutions are compared with the self-similar boundary layer solution. The velocity and temperature are normalized by corresponding freestream boundary condition, while y is nondimensionalized by $\sqrt{x\mu / \rho U}$ . Figure 6 illustrate that the results of the current numerical simulation agree very well with theoretical solutions. Thus second-order TVD scheme is accurate enough to be the supporting inlet condition of fifth-order shock-fitting method.

## V. Steady Flow over three-dimensional flat plate with Roughness

The three-dimensional roughness is mounted on the surface of plate at downstream $x = 0.185m$. Following Whiteheard's experiments (*2006*), the surface roughness is governed by the elliptic equation,

$$\frac{(x-Rap)^2}{a^2}+\frac{y^2}{b^2}+\frac{(z-L_\varsigma/2)^2}{c^2}=h^2 \tag{33}$$

Where $L_\varsigma$ is the spanwise length of flat plate. The computation are performed under parameter configuration $a = 2,\ b = 1, c = 1$ and $h/\delta = 1/2$ where $\delta$ corresponds to the boundary layer thickness at $x_c = 0.185m$ as shown in Figure 7.

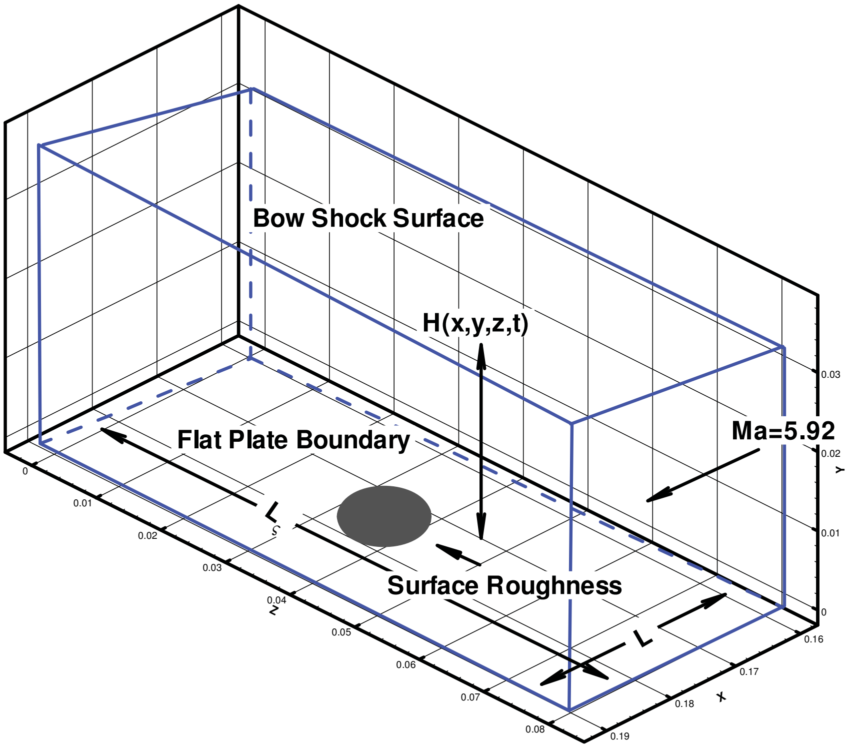

***Fig.7. Computational schematic of hypersonic flow over flat plate with finite surface roughness.***

In section III we discussed the methodology of treating irregular domain without roughness. A coordinate transformation is employed to simplify the computation. The optimal formation of transformation formula is determined by the specific physical model. For viscous flow simulation, two steps of mapping procedure could be implemented to obtain better resolution inside the viscous layer. The first step is involving transforming the entire physical domain under Cartesian coordinates into a square defined on $[0,1]\times[0,1]\times[0,1]$ under an intermediate coordinate space. The relation is defined as:

$$\begin{cases} X = \dfrac{x - x_{strart}}{L} \\ Y = \dfrac{y}{H(x,z)} \\ Z = \dfrac{z}{L_{\zeta}} \end{cases} \tag{34}$$

Where $(X,Y,Z)$ is defined under the intermediate coordinate system. $L$ is the streamwise length of the flat plate in current physical domain. $x_{start}$ is the physical streamwise coordinate of starting point of computation. The distance along $\eta$ between the solid wall and bow shock is referred to $H$.

In the second step of transformation, the intermediate plane $(X,Y,Z)$ is mapped into the computational domain $(\xi,\eta,\varsigma)$ in order to cluster more grids into the viscous layer on the flat plate. In present study, an exponential stretch function is employed as following,

$$\begin{cases} X=\xi \\ Y=-\dfrac{\left(\dfrac{\beta+1}{\beta-1}\right)^{(1-\eta)}-1}{\left(\dfrac{\beta+1}{\beta-1}\right)^{(1-\eta)}+1}\beta \\ Z=\varsigma \end{cases} \tag{35}$$

where $\beta$ is the stretching parameter. In current simulation $\beta=1.0$. The combination of the two steps leads to Eq. (11).

By substituting Eq. (52) into roughness surface function Eq. (10), the analytical equation for roughness in computational domain can be written as

$$f(\xi,\eta,\varsigma)=\frac{(L\xi)^2}{a^2}+\frac{\ell H(\xi L+x_{start},\varsigma L\varsigma)^2}{b^2}\frac{(\varsigma L_\varsigma-L/2)^2}{c^2}-h^2=0$$
$$\text{with } \ell=\frac{\left(\dfrac{\beta+1}{\beta-1}\right)^{(1-\eta)}-1}{\left(\dfrac{\beta+1}{\beta-1}\right)^{(1-\eta)}+1}\beta \tag{36}$$

An array of three dimensional roughnesses defined by relation (39) with mutual distance $L_\varsigma=0.0068m$ is placed on the flat-plate at $x_c=0.185m$ downstream from the leading edge. A periodic boundary condition is imposed in the z direction.

The 3-D simulation of hypersonic flow over roughness is conducted by using the cut cell method and up to third-order converging case is achieved. The total girds used for computing the zone contain roughness is $241\times121\times40$. The 3-D pressure and wall normal velocity contour is shown in Fig. 8. The hypersonic flow over the surface roughness generates a weak shock wave parallel to the roughness surface. Immediately after the weak shock wave, a 3-D expansion wave is generated and extend to downstream as in 2-D case. Controlled by the roughness shape, the shock strength reaches its maximum value in the middle of z direction and gradually decreases as moving to other two sides. Figure 8 (b) shows the normal velocity contour. A spanwise vortex is formed in the downstream of roughness, which is generated by the shear force as the flow passes the 3-D elliptic roughness surface. But the vortex shed rapidly due to the viscous dissipation close to the boundary layer.

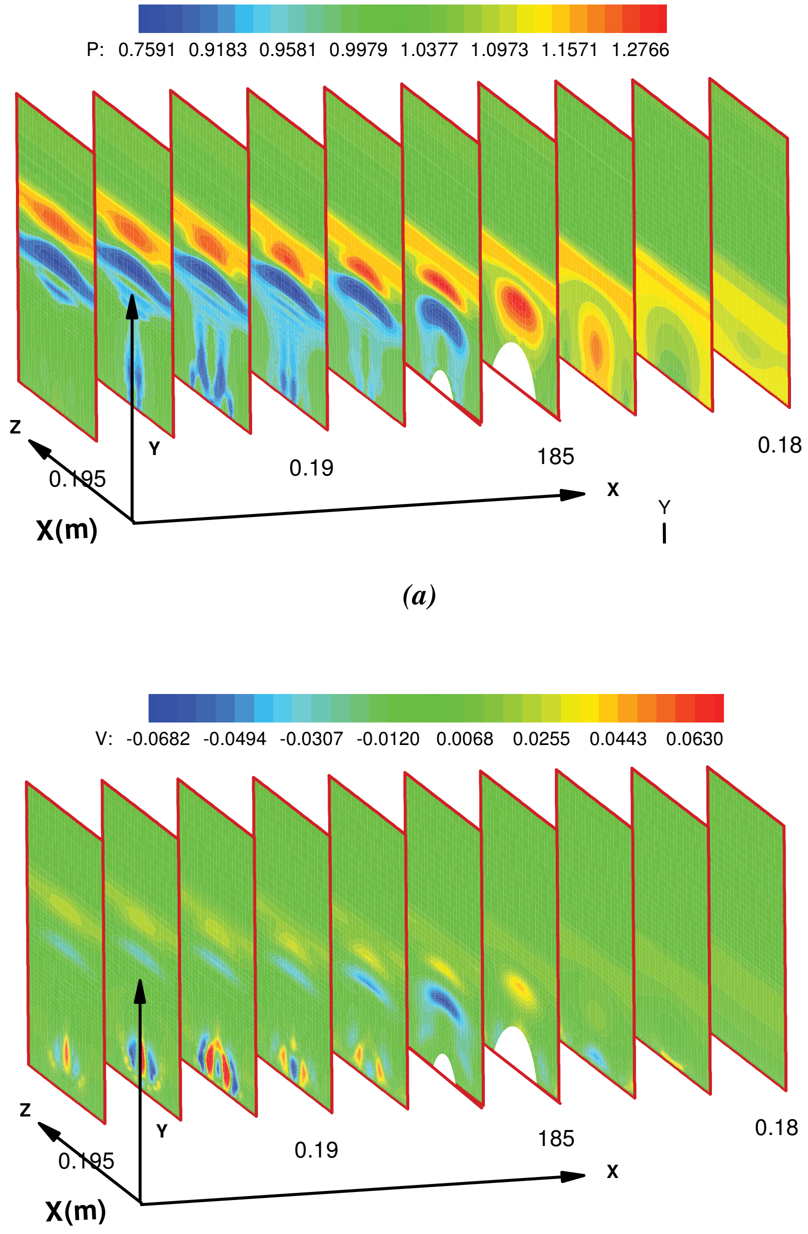

*(a)*

*(b)*

***Fig.8. Computational contour of 3-D hypersonic flow over flat plate with finite surface roughness.a), pressure b), wall normal velocity. girds :*** $241\times121\times40$.

Figure 9 shows 2-D spanwise velocity and streamline contour of hypersonic flow over flat plate with finite surface roughness in the x-z plane. Since the periodic boundary condition is imposed, the computational result is symmetry along the central lines across the roughness in the x direction. The streamline pattern shows with roughness element, the original flow field is modified significantly. The flow is separated into two branches equally as approaching the roughness front and then merge together after passing the roughness.

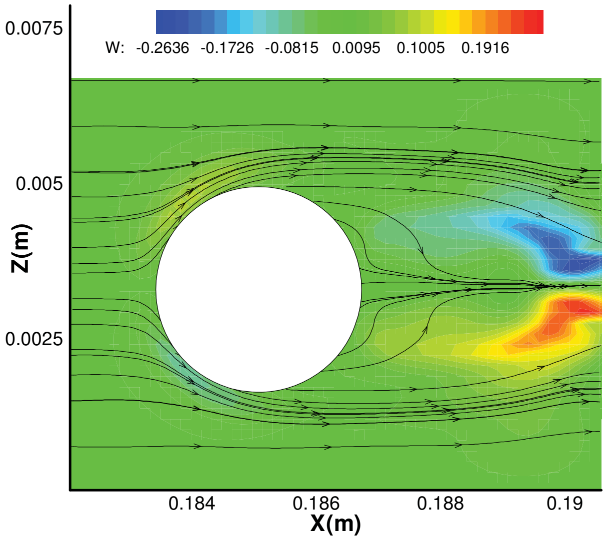

*Fig.9. 2-D spanwise velocity and streamline contour of hypersonic flow over flat plate with finite surface roughness. Black lines represent streamlines in x-z computational plane.*

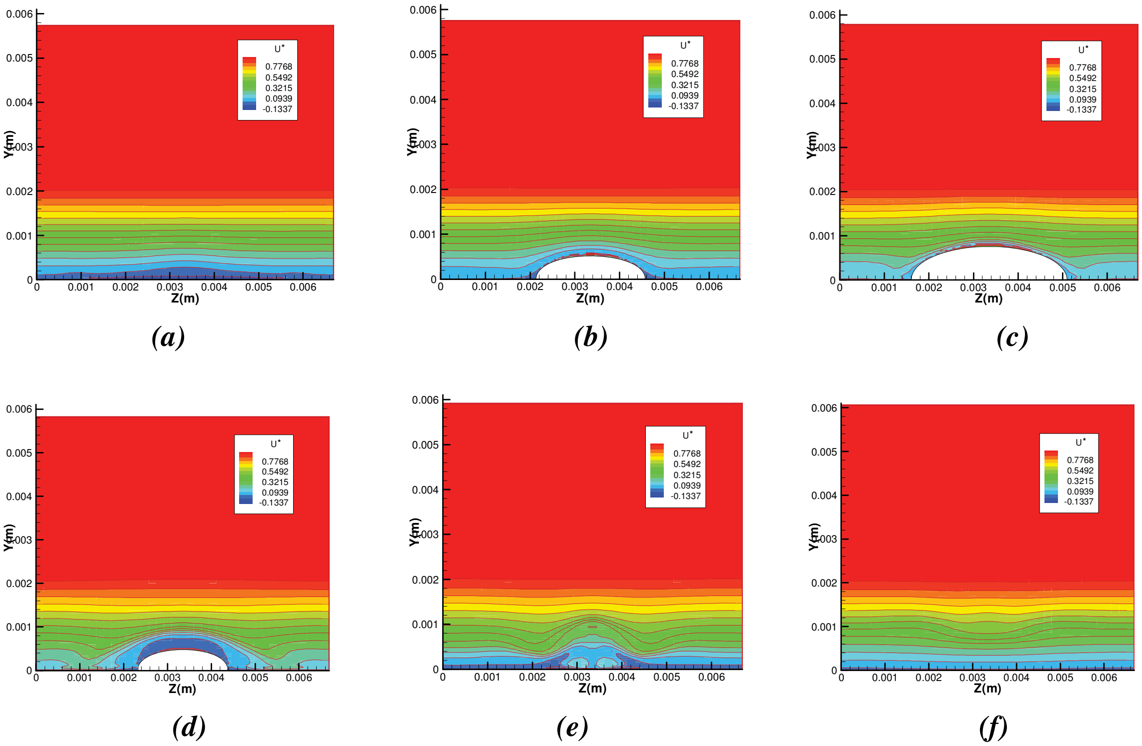

*(a)* *(b)* *(c)*

*(d)* *(e)* *(f)*

***Fig.10. 2-D streamwise velocity contour in x direction. a),*** $x = 0.1830m$ ***b),*** $x = 0.1838m$ ***c),*** $x = 0.1845m$ ***d),*** $x = 0.1860m$ ***e),*** $x = 0.1890m$ ***f),*** $x = 0.1950m$.

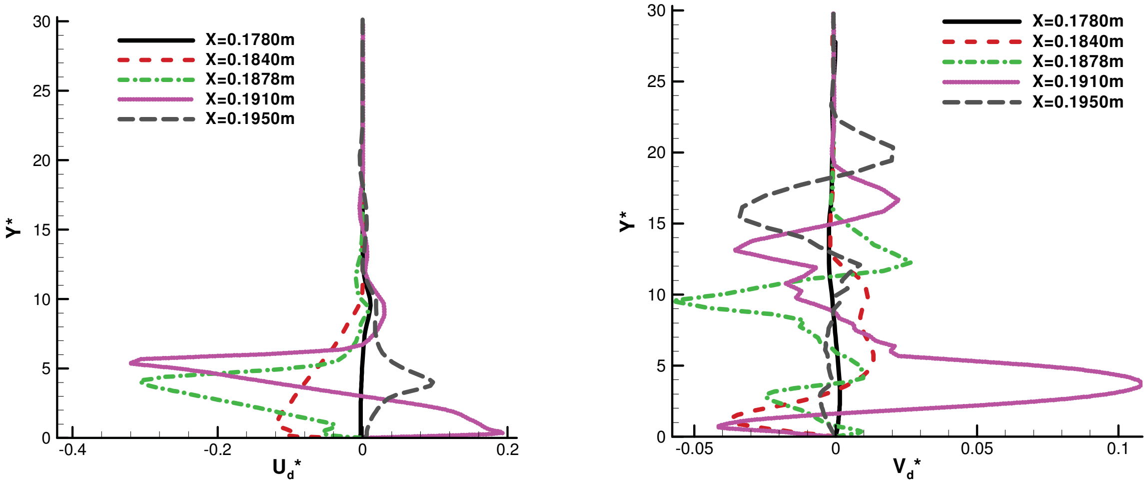

***Fig.11. Variation of velocity disturbance profile in x direction as difference between DNS solution and Blasius boundary layer solution. a), difference of streamwise velocity $U_d^*$ b), difference of wall-normal velocity $V_d^*$ along symmetry line.***

Figure 10 show the 2-D streamwise velocity variation in y-z plane along x direction. In the upstream of surface roughness, due to the roughness effect, boundary layer flow is minorly modified. In order to maintain the continuity of flow field, the streamline velocity approaches zero in small regions before the roughness. As the flow moves downstream and contacts with the surface roughness, a new boundary layer is formed on the roughness surface. As the flow moves to the roughness tail, the boundary layer is fully developed. In the region downstream of surface roughness, the roughness effect starts to modify the original boundary layer. A gap is formed immediately after the roughness where the pressure is relatively low. The gap is then filled rapidly by fluids surround. Thus due to the existence of surface roughness, the original homogenous boundary layer feathers are changed significantly as shown in fig 10 (e). At the end of current computational domain where $x = 0.1950m$, the velocity contain shows that the mean flow without roughness is restored.

Figure 11 show velocity disturbance profile along x direction as difference between DNS solution and Blasius boundary layer solution. Figure 11 (a) shows that difference of streamwise velocity $U_d^*$ along the symmetry line. As discussed in the last paragraph, the disturbance generated by roughness to the boundary layer is small before the roughness region, is amplified gradually in the roughness region, and is reduced to the mean Blasius solution in the region far downstream. This kind of disturbance behavior applies to Fig 11 (b), difference of wall-normal velocity too. The disturbance profile is modified significantly in the roughness region and back to original state in the far downstream. This implies that roughness only exert local effect to the boundary layer. The boundary layer instability feathers may not change in region far downstream of surface roughness.

## VI. Conclusion and Future Plan

A 3-D numerical test has been conducted to verify the high–order 3-D shock-fitting and cut-cell method. The new simulation is based on original configuration of the Mach 7.92 flows over flat-plate. An array of 3-D roughness is placed on the surface of plate at downstream $x = 0.185m$. The simulation results show that current cut-cell method is adequate in high-order numerically simulating the transition in boundary layer induced by surface roughness. The computational results show the after the roughness element, the mean flow is modified significantly by disturbances generated by the 3-D roughness. But in the far downstream of roughness, the mean flow profile is restored. The code is being developing and will be applied to numerically simulate the receptivity and transient growth of 3-D boundary layer with finite surface roughness.

## Acknowledgments

This work was sponsored by the AFOSR/NASA National Center for Hypersonic Research in Laminar-Turbulent Transition and by the Air Force Office of Scientific Research, USAF, under Grants No. FA9550-07-1-0414 and FA9550-04-1-0029, monitored by Dr. John Schmisseur. The views and conclusions contained herein are those of the authors and should not be interpreted as necessarily representing the official policies or endorsements either expressed or implied, of the Air Force Office of Scientific Research or the U.S. Government.

## References

1. **E. Piot, G. Casalis and M. Terracol , *Direct Numerical Solution of the Crossflow Instabilities Induce by a Periodic Roughness Array on a swept cylinder: receptivity and stability investigations*, 37th AIAA Fluid Dynamics Conference and Exhibit, Miami, FL, June 25-28, 2007 No. 1, 1999, pp. 134-150**

2. **S. Berry and T. Horvath, *Discrete Roughness Transition for Hypersonic Flight Vehicles* , 45th AIAA Aerospace Sciences Meeting and Exhibit, Reno, Nevada, Jan. 8-11, 2007**

3. **Malik, M.R., Spall, R. E., and Chang, C. L., *Effect of Nose Bluntness on Boundary Layer Stability and Transition.* 1990. AIAA Paper 90-0112.**

4. **William S.Saric, Helen L. Reed, and Edward J.Kerschen, *Boundary-Layer Receptivity to Freestream Disturbances*, Annu. Rev. Fluid Mech, 2002.34:291-319**

5. **Tani, I. *Boundary Layer Transition*, Annual Review of Fluid Mechanics, Vol.1, 1969, pp.169-196**

6. **P. Balakumar, *Transition in a Supersonic Boundary-Layer due to Roughness and Acoustic Disturbances*, AIAA 2003-3589**

7. **Ellingsen, T. and Palm, E., *Stability of Linear Flow*, Phys. Fluids, Vol. 18, No. 487, 1975.**

8. **Landahl, M. T., *A Note on an Algebraic Instability of Inviscid Parallel Shear Flows*, J. Fluid Mech., Vol.998,1980,pp. 243-251**

9. **Trefethen, L., Trefethen, A., Reddy, S., and Driscoll, T., *Hydrodynamic Stability without Eigenvalues*, Science, Vol. 261, 1993.**

10. **Henningson, D., *Bypass Transition and Linear Growth Mechanisms*, Advances in TurbulencV, edited, by R. Benzi, Kluwer, 1995.**

11. **Reshotko, E., *Transient Growth—A Factor in Bypass Transition,* Phys. Fluids, Vol. 13, No. 5, 2001, pp. 1067-1075.**

12. **Andersson, P., Berggren, M., and Henningson, D. S., *Optimal Disturbances and Bypass Transition in Boundary Layers*, Phys. Fluids, Vol. 11, No. 1, 1999, pp. 134-150.**

13. **Luchini, P., *Reynolds-Number-Independent Instability of the Boundary Layer over a Flat Surface: Optimal Perturbations*, J. Fluid Mech.,Vol. 404, 2000, pp. 289-309.**

14. **Tumin, A. and Reshotko, E., Spatial Theory *of Optimal Disturbances in Boundary Layers,* Phys. Fluids*,* Vol. 13, No. 7, 2001, pp. 2097-2104.**

15. **Morkovin, M. V., *On Roughness-Induced Transition: Facts, Views & Speculation*, Instability and Transition, edited by M. Y. Hussaini and R. G. Voight, Vol. 1, Springer, 1990, pp. 281-295.**

16. **Morkovin, M. V., *Panel Summary on Roughness,*Instability and Transition, edited by M. Y. Hussaini and R. G. Voight, Vol. 1, Springer, 1990, pp. 265-271.**

17. **Reshotko, E. and Leventhal, L., *Preliminary Experimental Study of Disturbances in a Laminar Boundary Layer Due to Distributed Roughness*, AIAA Paper 81-1224, 1981.**

18. **White, E. B., and Reshotko, E., *Roughness-Induced Transient Growth in a Flat-Plate Boundary Layer*, AIAA Paper 2002-0138, 2002.**
19. **White, E. B., *Transient Growth of Stationary Disturbances in a Flat Plate Boundary Layer, Physics* of Fluids, Vol. 14, No. 12, 2002, pp. 4429–4439.**

20. **White, E. B., and Ergin, F. G., *Receptivity and Transient Growth of Roughness-Induced Disturbances,* AIAA Paper 2003-4243, 2003.**

21. **White, E. B., Rice, J. M., and Ergin, F. G., *Receptivity of Stationary Transient Disturbances to Surface Roughness*, Physics of Fluids, Vol. 17, No. 6, 2005, 064109.**

22. **White, W.B., *Receptivitty of Transient Growth to Surface Roughness,* AIAA JOURNAL Vol. 44, No.11, November 2006**

23. **Kendall, J., *Laminar Boundary Layer Velocity Distortion by Surface Roughness: Effect upon Stability*, AIAA Paper 81-0195, 1981.**

24. **M. Choudhari, *Roughness-Induced Transient Growth,*_ 35th AIAA Fluid Dynamics Conference and Exhibit, Toronto, Ontario, June 6-9, 2005**

25. **P. Fischer, *Numerical Simulation of Roughness-Induced Transient Growth in a Laminar Boundary Layer*¸34th AIAA Fluid Dynamics Conference and Exhibit, Portland, Oregon, June 28-1, 2004 108**

26. **E. Piot, G. Casalis and M. Terracol, *Direct Numerical Solution of the Crossflow Instabilities Induced by a Periodic Roughness Array on a swept cylinder: receptivity and stability investigations,*_ 37th AIAA Fluid Dynamics Conference and Exhibit, Miami, FL, June 25-28, 2007**

27. **Donald P. Rizzetta; Miguel R. Visbal*, Direct Numerical Simulations of Flow Past an Array of Distributed Roughness Elements*¸ AIAA Journal 2007 0001-1452 vol.45 no.8 (1967-1976)**

28. **J.W.Purvis and J.E.Burkhalter, *Prediction of critical Mach number for store configurations* AIAA J. 17, 1979**

29. **D.K.Clarke, M.D.Salas, *Euler calculations for multielement airfoils using Cartesian grids* AIAA J.24, 1986**

30. **M.J.Berger and R.J.Leveque,** ***Stable Boundary Condition for Cartesian Grid Calculations*****, Computing System,1990**

31. **Hans Johansen, Phillip Colella*****, A Cartesian Grid Embedded Boundary Method for poisson's equation,*** **J. Comput. Phys, 1998**

32. **Pember, Bell, Colella et al.*****, An Adaptive Cartesian Grid Method for Unsteady Compressible Flow irregular Regions*****, J. Comput. Phys, 2006**

33. **Colella et al.,** ***A node-centered local refinement algorithm for Poisson's equation in complex geometries,*** **J. Comput. Phys,2004**

34. **James J. Quirk*****, An alternative to unstructured girds for computing gas dynamic flows around arbitrarily complex bodies*****, Comp. Fluids, 1994**

35. **T. Ye, R. Mittal, H. S. Udaykumar and W. Shyy,** ***An Accurate Cartesian Grid Method for Viscous Incompressible Flows with Complex Immersed Boundaries*****, Journal of Computational Physics,** ***Volum. 156, Issue 2*****,** ***10 December 1999*****,** ***Pages 209-240***

36. **Hans Forrer and Rolf Jeltschy ,** ***A Higher-Order Boundary Treatment for Cartesian-Grid Methods*** **, J. Comput. Phys, 1997**

37. **M,Popescu et al.,** ***A Finite Volume-Based High Order Cartesian Cut-cell Method for Computational Aeroacoustics,*** **AIAA Paper, 2005**

38. **Michael Barad, Phillip Colella*****, A fourth-order accurate local refinement method for poisson's equation*****, J. Comput. Phys, 2005**

39. **Gibou, Fedkiw*****, A fourth order accurate discretization for laplace and heat equations on arbitrary domain*****, J. Comput. Phys, 2004**

40. **DD.Zeeuw and KG.Powell,** ***An Adaptively Refined Cartesian Mesh Solver for the Euler Equations,*** **J. Comput. Phys, 1993**

41. **X.Zhong*****, High-order finite-difference schemes for numerical simulation of hypersonic boundary- layer transtion,*** **J. Comput. Phys 144 , 1998**

42. **J. H. Williamson, Low-storage Runge–Kutta schemes,** ***J. Comput. Phys.*** **35, 48 (1980).**

43. **A.H. Whitehead, Jr.** ***Flowfield and drag characteristics of several boundary-layer tripping elements in hypersonic flow. Techinical Note TND-5454, NASA October 1969***

44. **Le Duan, Xiaolin Zhong*****, A High Order Cut-Cell Method for Numerical Simulation of Three-Dimensional Hypersonic Boundary Layer Stability, submitted to 47th AIAA Aerospace and Science Meeting***

45. **Le Duan*****,*** **Xiaoweng Wang and Xiaolin Zhong,** ***A High Order Cartesian Girds Method for Numerical Simulation of Hypersonic Boundary Layer Stability With Finite Surface Roughness, AIAA-2008-3732, 38th Fluid Dynamics Conference and Exhibit, Seattle, Washington, June23-26, 2008***